DIPLOMA THESIS

Dynamical Mean-Field Theory for Hard-Core Bosons

submitted in satisfaction of the requirements for the degree of
Diplom-Ingenieur

Institute of Solid State Physics
Vienna University of Technology

under the supervision of
Associate Prof. Jan Kuneš, PhD

by

Dominik Huber, BSc

ID Number: 01326490

Wien, 24.03.2021

Prof. Jan Kuneš, PhD

Abstract

We formulate dynamical mean-field theory for hard-core bosons by extending bosonic DMFT with broken canonical commutation relations to use for $LaCoO_3$, amongst others. Pointwise convergence of results with finite on-site repulsion to results with explicit hard-core constraints is found by simulations of different models. Further we find, that a formulation analogous to Dyson-Mori form for fermions is not generally applicable for hard-core bosons due to a divergence at half filled lattice. Last we show a phase transition visible in the occupation of sublattices which can be driven by a change of coupling constants.

Contents

1 Motivation

The scientific field of modern solid-state physics comprises a wide variety of numerical techniques and analytical methods to treat numerous materials. One of the most active fields in condensed matter physics are correlated many-body systems, which are characterized by open d and f electron shells. The electrons in these narrow orbitals are strongly interacting and can therefore not be treated independently, like it is the case for the free electron gas. In this work we focus on new numerical technique to describe the physics of lanthanum cobalt oxide $LaCoO_3$.

1.1 $LaCoO_3$

Magnetic and transport properties of $LaCoO_3$ are under investigation since the 1960's. It crystallizes in perovskite structure, in which cobalt atoms bind to oxygen atoms and emerging Co^{3+} ions are responsible for the magnetic and transport properties [1]. Bulk $LaCoO_3$ at low temperatures is a non-magnetic insulator, but develops ferromagnetic (FM) order in strained films [2]. In the atomic picture Co^{3+} has a $3d^6$ configuration, which is strongly affected by the crystal field splitting. For octahedral symmetry electronic orbitals can be classified into T_{2g} and E_g symmetry (irreducible representation) with different energies, shown in figure 1.1.

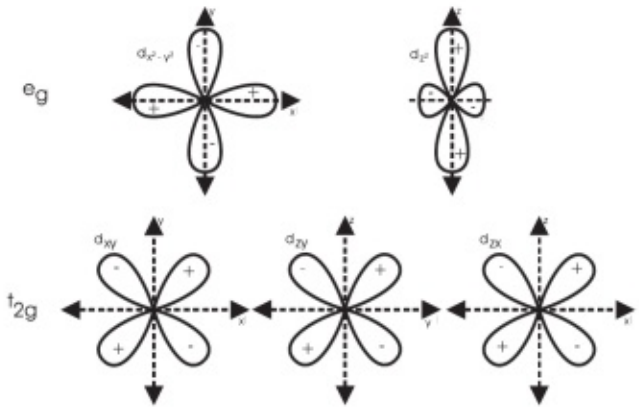

Figure 1.1: Electronic orbitals with quantum number l=2 (d orbitals) have five different shapes.

Without crystal field splitting distribution of electrons among the orbitals is dictated by Hund's rules, but if the separation of the E_g and T_{2g} levels gets big enough it is favorable to occupy T_{2g} levels first [3]. (See also figure 1.3). Due to this splitting the lowest many-body state of Co^{3+} ions has all T_{2g} orbitals occupied and non of the E_g orbitals. This is called the low spin state (LS) with total spin S=0. Dependence of the atomic multiplet energies on the crystal field splitting (Δ) is captured by so called Tanabe-Sugano diagrams. The diagram for d^6 configuration in octahedral crystal field is shown in figure 1.2. An excitation of an electron-hole pair forms an intermediate spin state (IS, S = 1), while the excitation of two electron-hole pairs forms a high spin state (HS, S = 2) (see figure 1.3).

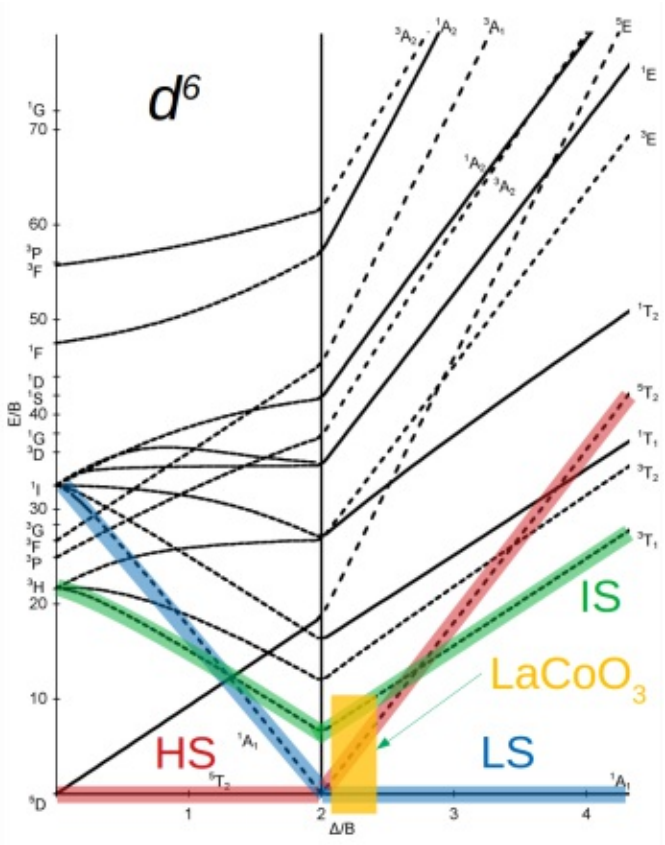

Figure 1.2: Tanabe-Sugano diagram [4] for d^6 electron configuration. The crystal field splitting for $LaCoO_3$ is larger than $\frac{\Delta}{B} = 2$ in the range of the colored area in the graph, and so the ground state is LS, HS has intermediate energy and IS high energy. B is a Racah parameter, which describes the electrostatic repulsion between electrons of the same atom [5].

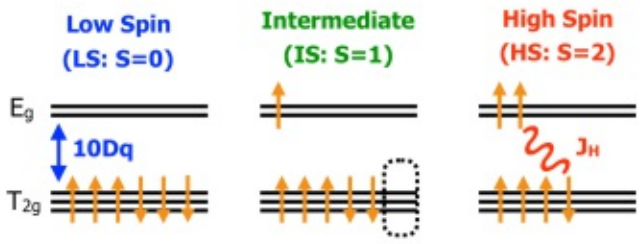

Figure 1.3: Orbital energy levels E_g and T_{2g} with different electron configurations and related spin quantum numbers S.

1.2 Experimental Results

The theoretical model building and simulation presented here is closely connected to resonant inelastic x-ray scattering (RIXS) experiments [6, 7]. To investigate the properties of $LaCoO_3$ single crystals were grown. See supplementary material of [6] and [7] for more detail. Results for RIXS measurements with different temperatures and x-ray momentum transfer q_c are shown in figure 1.4. The peak at $0.2-0.4\,\text{eV}$ corresponds to $LS \rightarrow IS$ excitation. Its dependence on the momentum transfer q_c implies that these excitations can not be viewed as local (atomic).

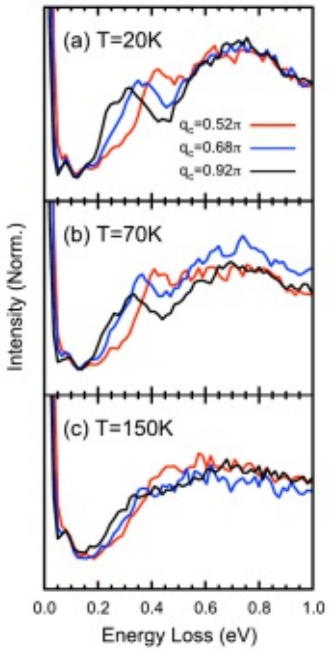

Figure 1.4: RIXS spectra for different temperatures and momentum transfer q_c [6]

1.3 Mobile IS Excitons

The dispersion of the peaks in figure 1.4 between 0.2 eV and 0.5 eV at $T = 20\,\mathrm{K}$ was explained recently with a new model. According to it the low temperature state of $LaCoO_3$ should be viewed as gas of mobile thermally excited excitons (IS) of several flavors (local orbital and spin structure) above (LS) vacuum [7]. Furthermore HS states behave as immobile biexcitons. A schematic picture of the lattice of LS background (small black points) occupied with IS excitons and HS biexcitons is shown in figure 1.5. Although HS states are strongly bound, fluctuations $|..., IS, IS, ...\rangle \leftrightarrow |..., LS, HS, ...\rangle$, give rise to dressed HS states. The IS and HS quasi-particles have integer spin and therefore obey boson statistics when spatially separated, but in this special case the underlying electrons have important impact. Two HS states, as well as two IS states of the same flavor at the same site are forbidden due to Pauli principle. Such quasi-particles are called hard-core (HC) bosons.
Further on chapter 2 will outline the construction of the model from d electron shells to LS, IS and HS HC bosons, and present the ingredients (boson and fermion statistics, HC bosons, Hubbard Model, Dynamical Mean Field Theory (DMFT)) for the simulation of a system of HC bosons on a lattice. The new approach in chapter 3 explains how quantities need to be rescaled to be used in bosonic DMFT with HC constraint. Chapter 4 shows results of bosonic DMFT with large (but finite) on-site repulsion of the bosons and compare them with calculations employing explicit HC constraint.

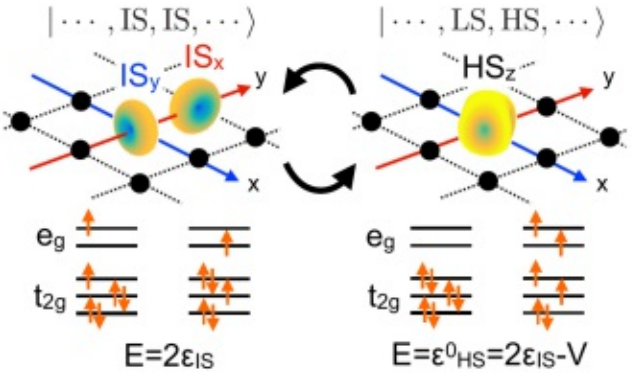

Figure 1.5: Mobile IS states (with directional propagation depending on their orbital character) are viewed as gas above LS vacuum. Two IS states with different flavor (x and y) at the same lattice site form stable immobile HS bi-excitons, but the spin fluctuation to next nearest neighbors is possible, which leads to dressed HS states [6].

2 Introduction

Physicists want to understand and predict properties of materials where Coulomb repulsion affects the motion of electrons in the solid. Therefore different simplifications of the full Hamiltonian have been developed, which take the essential properties into account and make calculation and simulation possible. As a benchmark, models have to fulfill the two extreme situations of the totally free electron gas and the totally localized electron at a particular atomic site. In the current work we use a model of HC bosons, therefore the outline of the construction and properties of bosons with HC constraint are discussed next.

2.1 Hard-Core Bosons

The construction of the HC boson model for $LaCoO_3$ in [2] consists of 3 main steps (see figure 2.1).

(A) A tight-binding (d-only) model is constructed and the local Coulomb interaction within the Co $3d$ shell is added, the O $2p$ orbitals are projected out.

(B) The 5-orbital model is reduced to a system of LS, IS and HS states. See also figure 1.5.

(C) The terms in model (B) are approximated so that lattice occupied by LS states represents a vaccum state, IS states are represented by mobile bosons (several flavors) and HS states are approximated as a local bi-exciton (a site occupied by two bosons of different flavor)

Once this model is obtained one has to learn how to calculate physical observables with this kind of particles. I will start with the definition of HC bosons in the mathematical sense.
Generally speaking physical particles and quasi particles are categorised in different ways related to the property one is interested in. Basic classification by spin degree of freedom distinguishes particles into fermions (spin quantum number S has half integer value; named after Enrico Fermi) and bosons (spin quantum number S has integer value; named after Satyendranath Bose [8]). They need to be

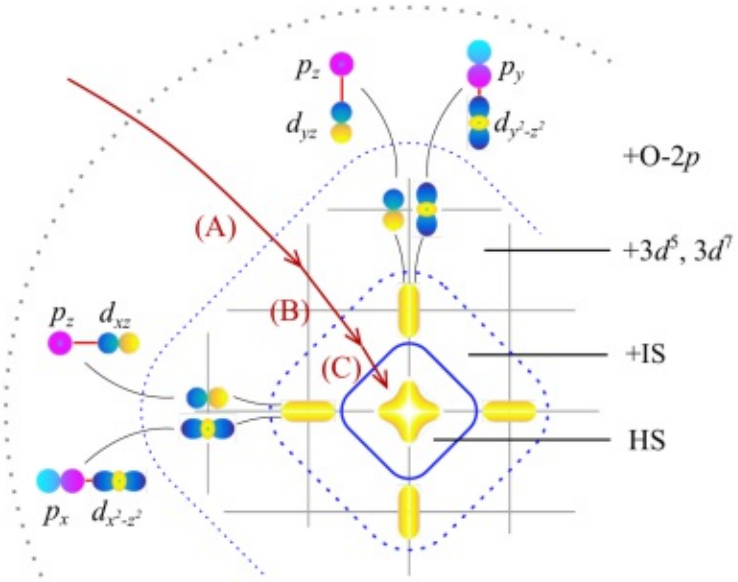

Figure 2.1: Construction of HC boson model for $LaCoO_3$ [2].

treated differently in statistical physics, as their distribution functions $n(\epsilon_p)$ differ, see equation 2.1 with positive sign in the denominator (fermions) and equation 2.2 with negative sign in the denominator (bosons). Where β is inverse temperature $\beta = \frac{1}{k_b T}$ with k_b the Boltzmann constant, μ is the chemical potential and ϵ_p is the single particle energy. The ways fermions and bosons occupy states are specified by these distribution functions, fermions obey Pauli principle and bosons do not. Fermions must differ at least by one quantum number, while bosons can occupy the same state with an arbitrary number of particles (see Bose-Einstein-Condensation [9])

$$n_F(\epsilon_p) = \frac{1}{e^{\beta(\epsilon_p - \mu)} + 1} \tag{2.1}$$

$$n_B(\epsilon_p) = \frac{1}{e^{\beta(\epsilon_p - \mu)} - 1} \tag{2.2}$$

Considering the wave like character of the particles, fermionic wave functions are fully anti-symmetric, while bosonic wave functions are fully symmetric. This is represented in second quantized form via canonical (anti-)commutation relations. Fermions obey anti-commutation relation $\{A, B\}$, equation 2.3, while bosons obey commutation relation $[A, B]$, equation 2.4. A and B are operators. $c_i^{(\dagger)}$ are fermionic annihilation (creation) operators and $b_i^{(\dagger)}$ are bosonic annihilation (creation) operators, respectively

Fermions:

$$\begin{aligned} \{A, B\} &= AB + BA \\ \{c_i, c_j\} = \{c_i^\dagger, c_j^\dagger\} &= 0 \\ \{c_i^\dagger, c_j\} &= \delta_{ij} \end{aligned} \tag{2.3}$$

Bosons:

$$\begin{aligned} [A, B] &= AB - BA \\ [b_i, b_j] = [b_i^\dagger, b_j^\dagger] &= 0 \\ [b_i, b_j^\dagger] &= \delta_{ij} \end{aligned} \tag{2.4}$$

The quasi particles we deal with in our treatment do have integer spin (electron-hole pair) but consist of underlying electrons with half integer spin. These so called hard-core bosons need special treatment, as it is forbidden, that two of the same flavor occupy the same lattice site. The canonical commutation relation in equation 2.4 transform to HC relations in each flavor in equation 2.5 with occupation number operator $n_i = b_i^\dagger b_i$
HC Bosons:

$$\begin{aligned} [b_i, b_j] = [b_i^\dagger, b_j^\dagger] &= 0 \\ [b_i, b_j^\dagger] &= \delta_{ij}(1 - 2n_i) \end{aligned} \tag{2.5}$$

In difference to fermions, where Pauli principle is fulfilled independently of the chosen basis, HC bosons are affected by unitary transformation of the commutation relation, described by Ortiz in chapter 17 in [10].
Next we will talk about fermions as historically the explained methods where developed for electrons. Later, we will explain the adaptions needed for bosons and HC bosons.

2.2 Hubbard Model

In 1963 J. Hubbard developed a model to describe systems with partially filled narrow energy bands, for example open d and f electron shells [11]. The dynamics of the electrons are summarized in the Hubbard Hamiltonian (equation 2.6), which contains two competing terms representing the core of the electronic many-body problem. On one side the kinetic energy $H_{kinetic}$ part favors the electrons to move between atoms, on the other side the interaction term $H_{interaction}$ leads to electrons that stay apart from each other, localized on atomic different sites. The model is defined on a lattice, which represents the crystal structure, where i and j are site

indices. Every site is the position of an atomic core of the investigated material. Electrons can hop from site to site via $H_{kinetic}$ since $c_{j\sigma}$ annihilates an electron at site j with spin σ and $c^{\dagger}_{i\sigma}$ creates an electron at site i with spin σ. Atomic sites can only be occupied by a maximum of one electron per spin direction (Pauli principle). This leads to four possibilities:

i) empty site "$\cdot\cdot$"

ii) occupied with up electron "$\uparrow\cdot$"

iii) occupied with down electron "$\cdot\downarrow$"

iv) occupied with up and down electrons "$\uparrow\downarrow$"

The summation runs over nearest neighbors, indicated by $\langle i,j\rangle$. t_{ij} is the hopping (or transition) amplitude. $H_{interaction}$ describes a repulsion of two electrons at the same site, if the on-site interaction U is positive. The occupation number operator $n_{i\sigma} = c^{\dagger}_{i\sigma}c_{i\sigma}$ is used to check if site i is populated. This repulsion effectively reduces electrons in the ground state. With an additional third term including the chemical potential μ the number of particles in the system can be controlled: $H_{\mu} = \mu \sum_{i\sigma} n_{i\sigma}$.

$$\begin{aligned} H_{Hubbard} &= H_{kinetic} + H_{interaction} \\ &= -\sum_{\langle i,j\rangle,\sigma} t_{ij} c^{\dagger}_{i\sigma} c_{j\sigma} + U \sum_{i} n_{i\uparrow} n_{i\downarrow} \end{aligned} \tag{2.6}$$

Although this model was developed for fermions first, it can also be used for bosons with small adaptions. This leads to the Bose-Hubbard model in equation 2.7. $b^{\dagger}_{i}$ and b_j are creation and annihilation operators for bosons at site i and j. With this Hamiltonian an atomic site can be occupied by an arbitrary number of particles. To implement the hard-core constraint dynamically we tune on-site interaction parameter U to high values, which makes it very unlikely for the system to occupy the same site with more than one particle. Tuning on-site interaction and comparison with explicit hard-core constraint is discussed in chapter 4.

$$H = -t \sum_{<i,j>} b^{\dagger}_{i} b_j + \frac{U}{2} \sum_{i} n_i (n_i - 1) \tag{2.7}$$

2.3 Dynamical Mean Field Theory

Since more than 30 years the very successful DMFT leads to big progress in our understanding of strongly correlated systems. "Dynamical mean field theory"

means that fluctuations on different lattice sites are uncorrelated while local (on-site) fluctuations are temporarilly correlated, in difference to Weiss mean field theory and Hartree-Fock approximation.

2.3.1 DMFT Approximation

Within DMFT the lattice model (in our case the Bose-Hubbard model) gets replaced by a single-site quantum impurity problem embedded in an effective medium [12]. Mapping of the Hubbard model onto a single impurity Anderson model in the limit of infinite dimensions ($d \to \infty$) was first implemented by Georges and Kotilar [13] soon after Metzner and Vollhardt showed that even in the limit of infinite dimensions the Hubbard model describes nontrivial correlations between fermions [14]. For review of fermionic DMFT see [15] where the mathematical descriptions are presented. We directly refer to bosonic DMFT in figure 2.2. The lattice model on the left hand side (described by the Hamiltonian 2.7) is translated into the appropriately defined impurity problem on the right hand side with impurity action S_{imp} (equation 2.8). The impurity site in thermal equilibrium can be described by propagation in imaginary time τ from 0 to inverse temperature β. During this period transitions between the impurity and the bath of normal bosons are determined by the hybridization function $\mathbf{\Delta}(\tau)$. Additionally to fermionic DMFT, transitions between the impurity and the bath of condensed bosons described by the condensate order parameter $\mathbf{\Phi}$ can appear. Where $\mathbf{\Phi}^\dagger = (\phi^\dagger, \phi)$ and annihilation and creation operators $\mathbf{b}^\dagger = (b^\dagger, b)$ are written in Nambu notation. Third and fourth term of S_{imp} describe the local physics of to Bose-Hubbard model equation 2.7.

$$\begin{aligned} S_{imp} = &-\frac{1}{2}\int_0^\beta \int_0^\beta d\tau\, d\tau' \mathbf{b}^\dagger(\tau)\mathbf{\Delta}(\tau-\tau')\mathbf{b}(\tau') - \kappa\mathbf{\Phi}^\dagger \int_0^\beta d\tau \mathbf{b}(\tau) \\ &- \mu\int_0^\beta d\tau n(\tau) + \frac{U}{2}\int_0^\beta d\tau n(\tau)[n(\tau)-1] \end{aligned} \tag{2.8}$$

We use the same definition of the hybridisation matrix as is used in [16]:

$$\mathbf{\Delta}(\tau-\tau') = \begin{pmatrix} F(\tau'-\tau) & 2K(\tau-\tau') \\ 2K^*(\tau-\tau') & F(\tau-\tau') \end{pmatrix} \tag{2.9}$$

The diagonal element of the hybridization function $F(\tau-\tau')$ is the transition amplitude for normal bosons. A boson is created at the impurity site at time τ' (taken from the bath) and annihilated at time τ (returned to the bath). The off-diagonal element $K(\tau-\tau')$ describes the process of creating two bosons at different times τ and τ'. Remaining factor κ depends on the lattice structure via the coordination number z (the number of neighboring sites) and on diagonal and

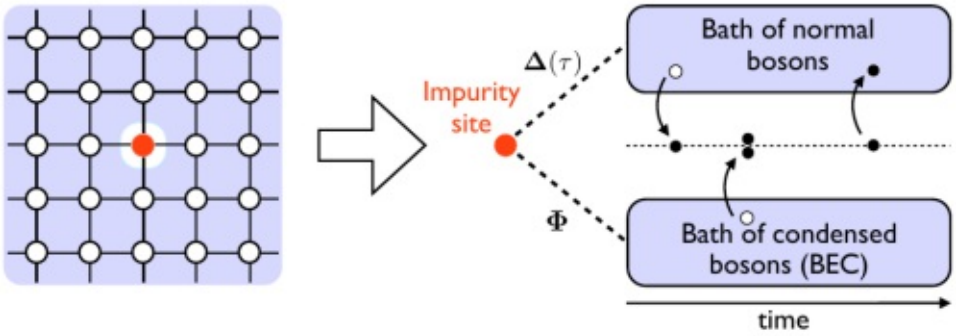

Figure 2.2: The lattice problem is mapped to a single site impurity model. During time evolution particles can hop between impurity site, normal and condensed reservoir. The DMFT approximation simplifies in that way, that spacial correlations are neglected but local interactions are treated exactly [16].

off-diagonal elements of the hybridization function and describes the coupling of the condensate to the normal bosons, see equation 2.21.

2.3.2 DMFT Cycle

Measurable observables can be calculated by using the impurity action S_{imp}, for example the local propagator (Green's function) and the condensate order parameter:

$$\mathbf{G}(\tau) = -\langle T\ \mathbf{b}(\tau)\mathbf{b}^{\dagger}(0)\rangle_{S_{imp}} \tag{2.10}$$

$$\mathbf{\Phi} = \langle \mathbf{b}(\tau)\rangle_{S_{imp}} \tag{2.11}$$

Here, T is the time ordering symbol and angle brackets denote quantum mechanical expectation values. Aim of the calculations are the diagonal and off-diagonal elements of the Green's function $\mathbf{G}(\tau)$, where diagonal ones represent the probability amplitude of creating a particle on the impurity site at one particular time and annihilating it after a time τ. Off-diagonal elements are again responsible for two particle processes. The condensate order parameter is the second important quantity, which represents the amplitude of transition of bosons between the impurity site and the bath of condensed bosons. To compute $\mathbf{G}(\tau)$ one needs to know $\mathbf{\Delta}(\tau), \Phi$ and κ, which are unknown a priori and obtained in a self consistent manner. This leads to the DMFT cycle shown in figure 2.3. Starting at the upper right position one needs initial values for $\mathbf{\Delta}(\tau), \Phi$ and κ. They can be gathered via (static) mean field theory, but also the trivial case is common: Setting the hybridization function to zero and condensate order parameter unequal zero, if

one expects condensate or equal zero, if one does not. Almost all of the computational effort is concentrated in the "Impurity Solver", the next step of DMFT self consistency loop. This is due to the difficult calculation of the quantum mechanical expectation value referred to S_{imp} in equation 2.12. The trace (Tr) leads to summation of all possible configurations of the system, where Z is the partition function. It is impossible to solve equation 2.12 exactly as the number of states in the observed quantum system grows exponentially with system size (which is infinite in priniciple). Therefore subtle methods were developed to find approximate solutions. We use a continuous time quantum Monte Carlo (CT-QMC) algorithm. Further information for the fermionic algorithm [17] and more general cases including improved estimators for faster convergence of the quantities in self consistency loop can be found elsewhere [18, 19]. The technical implementation of CT-QMC leads to use of imaginary time (τ) representation of the measured quantities.

$$\langle A \rangle = \frac{1}{Z} \operatorname{Tr} A e^{-\beta H} \tag{2.12}$$

CT-QMC impurity solver provides results for $\mathbf{G}(\tau)$, which is the propagator for normal and condensed bosons, and for $\mathbf{\Phi}$. With this we obtain the so called connected part of the Green's function (for normal bosons only) via

$$\mathbf{G}_c(\tau) = \mathbf{G}(\tau) + \mathbf{\Phi}\mathbf{\Phi}^\dagger. \tag{2.13}$$

For the following steps the quantities need to be transformed into Fourier space referred to Matsubara frequency $\omega_n = 2\pi n/\beta$, a mesh that is proportional to temperature (n is integer). Connected part $\mathbf{G}_c(i\omega_n)$ can be found in the lower left of the DMFT cycle (figure 2.3), so that half of the loop is reached. Dyson equation is used next to determine self energy

$$\mathbf{\Sigma}(i\omega_n) = \mathbf{G}_0^{-1}(i\omega_n) - \mathbf{G}_c^{-1}(i\omega_n). \tag{2.14}$$

Here, $\mathbf{G}_0^{-1}(i\omega_n)$ is the bare Green's function, which itself is calculated via hybridization function

$$\mathbf{G}_0^{-1}(i\omega_n) = \mathbf{\Delta}(i\omega_n) + i\omega_n \boldsymbol{\sigma}_3 + \mu\mathbf{I}. \tag{2.15}$$

Hence DMFT approximation, where self energy loses its momentum dependence $\Sigma(\mathbf{k}, i\omega_n) = \Sigma(i\omega_n)$, allows to calculate the k-summed (local) lattice Green's function

$$\mathbf{G}_{latt}(i\omega_n) = \sum_{\mathbf{k}} [i\omega_n \boldsymbol{\sigma}_3 + (\mu - \epsilon_{\mathbf{k}})\mathbf{I} - \mathbf{\Sigma}(i\omega_n)]^{-1}, \tag{2.16}$$

The lattice properties enter via the dispersion $\epsilon_{\mathbf{k}} = -\sum_{ij} t_{ij} e^{i\mathbf{k}(\mathbf{R}_i - \mathbf{R}_j)}$ where the hopping parameter t_{ij} and the distance between sites are included. Also the transformation of the summation over wave vectors into an integration over the density of states $D(\epsilon) = \sum_{\mathbf{k}} \delta(\epsilon - \epsilon_{\mathbf{k}})$ can lead to simplifications under the right circumstances:

$$\mathbf{G}_{latt}(i\omega_n) = \int d\epsilon D(\epsilon)[i\omega_n \boldsymbol{\sigma}_3 + (\mu - \epsilon)\mathbf{I} - \boldsymbol{\Sigma}(i\omega_n)]^{-1} \tag{2.17}$$

A Hilbert transformation is needed to compute k summed lattice Greens function, because the integral is only defined using Cauchy principal value. This is done element wise with

$$\boldsymbol{\Sigma} = \begin{pmatrix} \Sigma & \tilde{\Sigma} \\ \tilde{\Sigma} & \Sigma^* \end{pmatrix} \quad \mathbf{G}_{latt} = \begin{pmatrix} G_{latt} & \tilde{G}_{latt} \\ \tilde{G}_{latt} & G_{latt} \end{pmatrix} \tag{2.18}$$

and leads to

$$\begin{aligned} G_{latt} &= \int d\epsilon D(\epsilon) \frac{(i\omega_n + \mu - \Sigma)^* - \epsilon}{|i\omega_n + \mu - \Sigma(i\omega_n) - \epsilon|^2 - \tilde{\Sigma}^2} \\ \tilde{G}_{latt} &= \int d\epsilon D(\epsilon) \frac{\tilde{\Sigma}}{|i\omega_n + \mu - \Sigma(i\omega_n) - \epsilon|^2 - \tilde{\Sigma}^2} \end{aligned} \tag{2.19}$$

By inserting equation 2.15 into equation 2.14 and rearranging for $\boldsymbol{\Delta}(i\omega_n)$ we find the updated hybridization function. Now the new obtained lattice (local) Green's function $\mathbf{G}^{-1}_{latt}(i\omega_n)$ is used. Also new κ is now calculated with the coordination number z and the hopping parameter t assumed to be isotropic.

$$\boldsymbol{\Delta}(i\omega_n) = -i\omega_n \boldsymbol{\sigma}_3 - \mu\mathbf{I} + \boldsymbol{\Sigma}(i\omega_n) + \mathbf{G}^{-1}_{latt}(i\omega_n) \tag{2.20}$$

$$\kappa = zt - \Delta_{11}(i\omega_n = 0) - \Delta_{12}(i\omega_n = 0) \tag{2.21}$$

A Fourier back transformation brings the quantities into imaginary time space and completes the DMFT cycle. This procedure is performed until convergence. The tools bosonic DMFT supplies are extended to hard-core constraints and mathematical details are shown in chapter 3.

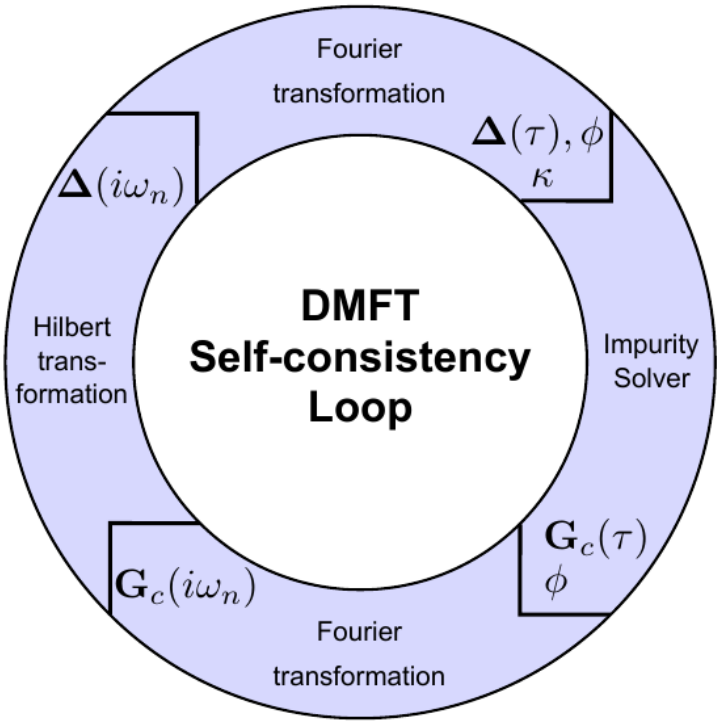

Figure 2.3: Schematic of the DMFT self consistency cycle [16]

3 Theory

Violating canonical commutation relation by the use of HC constraint for bosons becomes problematic for the calculation of self energy via Dyson equation 2.14 in DMFT cycle, since the HC propagator does not follow the asymptotic $1/\omega$ behavior of the canonical one. Moreover the diagrammatic techniques, developed for canonical bosons (and fermions) cannot be applied directly for HC particles. Therefore we adopt the view that HC bosons are obtained as canonical bosons in the limit of on-site repulsion $U \to \infty$ between bosons of the same flavor. The spectrum of canoncial bosons (figure 3.1) yields an insight to this limit. It can be divided into a low-energy part $\bar{\mathbf{A}}$ (gray), with vanishing U-dependence, and into a high-energy part $\mathbf{a}$ (red) with the lower bound roughly around U

$$\mathbf{A}(\omega) = \bar{\mathbf{A}}(\omega) + \mathbf{a}(\omega) \tag{3.1}$$

and the same is done for corresponding Greens function

$$\mathbf{G}(\omega) = \bar{\mathbf{G}}(\omega) + \mathbf{g}(\omega) \tag{3.2}$$

while they are connected via the spectral representation

$$\mathbf{G}(\omega) = \int d\nu \frac{\mathbf{A}(\nu)}{\omega - \nu}. \tag{3.3}$$

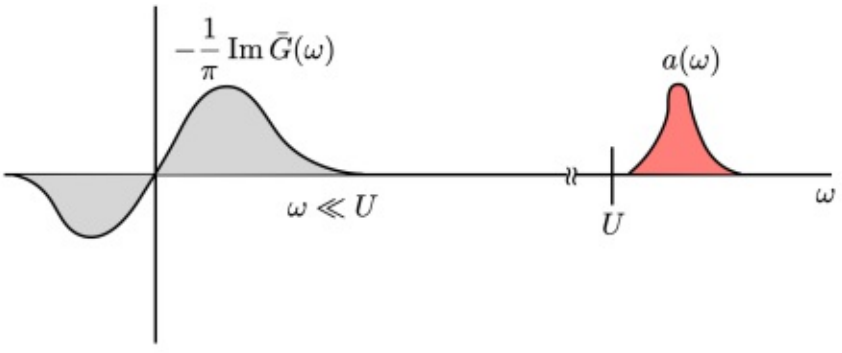

Figure 3.1: Representative spectral density of canonical bosons

For the HC limit $\bar{\mathbf{G}}$ reduces to the solution of the hard-core problem. Using the fact, that for large U only the total weight of the upper Hubbard band $\mathbf{a}(\omega)$, but not the shape, plays a role

$$|\mathbf{g}(\omega)| = \left| \int_0^\infty d\nu \frac{\mathbf{a}(U+\nu)}{\omega - U - \nu} \right| \leq \left| \frac{\int d\nu \mathbf{a}(\nu)}{\omega - U} \right| \tag{3.4}$$

we show that $\mathbf{G}^{-1} \approx \bar{\mathbf{G}}^{-1}$ for $\omega \ll U$. To this end we multiply equation 3.2 with $\bar{\mathbf{G}}^{-1}$ from the left and with $\mathbf{G}^{-1}$ from the right. Products $\mathbf{G}\mathbf{G}^{-1}$ cancel and one arrives at

$$\bar{\mathbf{G}}^{-1}(\omega) - \mathbf{G}^{-1}(\omega) \approx \bar{\mathbf{G}}^{-1}(\omega)\mathbf{g}(\omega)\bar{\mathbf{G}}^{-1}(\omega) = o\left(\frac{1}{U}\right) \tag{3.5}$$

$$\left|\bar{\mathbf{G}}^{-1}(\omega) - \mathbf{G}^{-1}(\omega)\right| \lim_{U\to\infty} = 0 \tag{3.6}$$

where only linear term in series expansion of $\mathbf{G}^{-1}$ is used. Then the matrix form of lattice Dyson equation 2.16

$$\mathbf{G}^{-1}(\omega) = \omega\mathbf{I} - \mathbf{h}_{loc} - \mathbf{\Delta}(\omega) - \mathbf{\Sigma}(\omega) \tag{3.7}$$

yields canonical self energy of the impurity problem, where $\mathbf{h}_{loc}$ is the local Hamiltonian of the impurity site. Substituting $\bar{\mathbf{G}}^{-1}$ for $\mathbf{G}^{-1}$ and solving for self energy leads to a result valid only for frequencies much smaller than U.

$$\mathbf{\Sigma}(\omega) = \omega\mathbf{I} - \mathbf{h}_{loc} - \mathbf{\Delta}(\omega) - \bar{\mathbf{G}}^{-1}(\omega); \quad \omega \ll U \tag{3.8}$$

With this we found a solution for the initial problem and DMFT cycle can be closed with

$$\mathbf{G}_k(\omega) = (\underline{\bar{\mathbf{G}}}^{-1}(\omega) + \underline{\mathbf{\Delta}}(\omega) + \underline{\mathbf{h}}_{loc} - \mathbf{h}_k)^{-1}\ ; \quad \omega \ll U \tag{3.9}$$

The underline notation $\underline{X} = \mathrm{diag}[X_1, X_2, \ldots]$ is used here for block-diagonal matrices which is necessary for systems with more than one impurity site within unit cell.
Referring to Shastry [20, 21], who worked on t-J model for fermions, we bring equation 3.9 into Dyson-Mori form. To this end a rescaling factor $\mathbf{\Gamma}$ is introduced

$$\mathbf{\Gamma} \equiv -\frac{1}{\pi}\int_{-\infty}^{\infty} d\omega \Im\bar{\mathbf{G}}(\omega) = 1 - \int_{-\infty}^{\infty} d\omega \mathbf{a}(\omega) \tag{3.10}$$

and can be calculated in the τ-representation of $\bar{\mathbf{G}}$ via

$$\mathbf{\Gamma} = \bar{\mathbf{G}}(\beta^-) - \bar{\mathbf{G}}(0^+). \tag{3.11}$$

We require for the following derivation, that $\Gamma \neq 0$, as it is necessary to calculate the inverse. In other words we demand that there exists a $1/\omega$ term in the series expansion of HC Greens function

$$\bar{\mathbf{G}}(\omega) \approx \frac{\Gamma}{\omega} + o\left(\frac{1}{\omega^2}\right). \tag{3.12}$$

Starting with equation 3.7 and modifying as

$$\bar{\mathbf{G}}^{-1}(\omega) = \mathbf{\Gamma}^{-1}\omega - \mathbf{h}_{loc} - \mathbf{\Delta}(\omega) - \mathbf{\Gamma}^{-1}\bar{\mathbf{\Sigma}}(\omega) \tag{3.13}$$

makes the comparison of 3.7 and 3.13 possible and shows the simple relation between canonical $\mathbf{\Sigma}$ and auxiliary $\bar{\mathbf{\Sigma}}$ self energy

$$\mathbf{\Gamma}^{-1}(\omega - \bar{\mathbf{\Sigma}}(\omega)) = \omega - \mathbf{\Sigma}(\omega)\ ; \quad \omega \ll U. \tag{3.14}$$

Substituting this relation to lattice Dyson equation leads to

$$\mathbf{G}_k(\omega) = \left(\omega\mathbf{I} - \underline{\mathbf{\Gamma}}\mathbf{h}_k - \underline{\bar{\mathbf{\Sigma}}}(\omega)\right)^{-1}\underline{\mathbf{\Gamma}} \tag{3.15}$$

which is a possible implementation of DMFT cycle, as $\bar{\mathbf{\Sigma}}$ and $\mathbf{\Gamma}$ are directly measured in CT-QMC impurity solver. It will also be shown, that the numerical treatment of $\bar{\mathbf{G}}$ is substantially easier than that of $\mathbf{G}$. Similarly $\bar{\mathbf{\Sigma}}$ reaches its asymptotic behavior outside the support of $\bar{\mathbf{G}}$, while the asymptotic behavior of $\mathbf{\Sigma}$ is reached first for $\omega > U$.
We will discuss the case of $\Gamma = 0$ in sub-section 4.2.1. This case is only problematic with Dyson-Mori form for bosons, but no physical uncertainty appears and therefore a solution can be found with the general lattice Dyson equation 3.9.

4 Results

Within this HC bosonic DMFT (HB-DMFT) project I did calculations with the CT-QMC impurity solver, which Atsushi Hariki implemented following Anders and Gull [22]. This is done to show the convergence of results with dynamical HC constraints (canonical bosons with finite value of on-site repulsion U) to the ones with explicit HC constraints explained in section 2.1 and chapter 3. We start with state of the art results from [2] and [6] where the rescaling factor $\Gamma = 1 - 2\langle n \rangle$ comes into Greens function as scalar due to the degeneracy of bosonic bands.

$$G_{\mathbf{k}} = \frac{\Gamma}{i\omega_n - \Gamma\varepsilon_{\mathbf{k}} - \Sigma(i\omega_n)} \tag{4.1}$$

Our goal is to show the convergence for HC constraints in full matrix form $\underline{\mathbf{\Gamma}}$ of equation 3.15. We will not study the cases with condensate here.
The dimension of the system is not an important parameter in DMFT, therefore next sections will treat models with different dimensions. Furthermore it is shown also in [2] and [6], that qualitatively it is irrelevant if one treats two or three excitonic orbital flavors even though the number of possible bi-excitons changes from one to three. Respective lattice is discussed in the sections with sketch and Hamiltonian.
A general convention is made for the notation of energies. Energy of the LS vacuum background is set to 0. The energies of IS excitons ε_α are parameters for respective models, where $\alpha \in \{1, 2\}$ being the index of the orbital flavor. On-site attraction V_s between excitons of different orbital flavor is the second energy that appears in the Hamiltonians, with s being the index of the atomic site in the unit cell. The more natural energy of HS bi-excitons $\mathcal{E}_s$ will also be used in the discussion and is calculated as $\mathcal{E}_s = \varepsilon_1 + \varepsilon_2 - V_s$. It is the resulting energy when two excitons of different orbital flavor couple via V_s to a bi-exciton.

4.1 Degenerate Exciton Energy Levels

First, data similar to the model in [6] where a cubic lattice is used with LS, IS and HS is reproduced. Here two orbital flavors of IS states are used instead of three in the cited source. Figure 4.1 sketches the lattice. Dimension is wrapped in $\mathbf{i} = i(1,0,0) + j(0,1,0) + l(0,0,1)$ with $i, j, l \in \mathbb{Z}$. The unit cell contains a

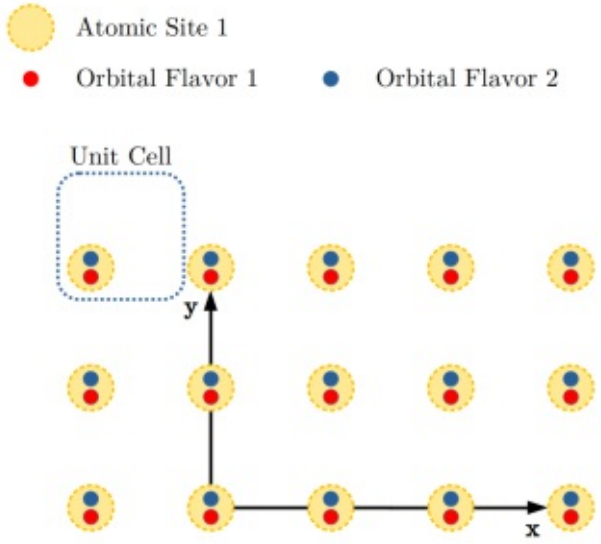

Figure 4.1: Sketch of the xy-plane of the lattice. There is a single atomic site per unit cell and excitations can either populate orbital flavor 1 (red) or flavor 2 (blue). IS excitons can either move along x- or y-axes, restricted to their orbital flavor, and z-direction, while HS bi-excitons can only move along z-axes perpendicular to the presented plane.

single atomic site where bosons can populate two different orbitals. Propagation direction[1] is orbital depending, so bosons in orbital 1 can move along y- and z-axes while bosons in orbital 2 are restricted to x- and z-axes. The resulting bi-exciton from combination of two excitons can propagate only in z direction perpendicular to the presented plane. Equation 4.2 shows the Hamilton operator we are working with.

$$H = \varepsilon \sum_{\mathbf{i}} \sum_{\alpha} n_{\mathbf{i},\alpha} - V \sum_{\mathbf{i}} n_{\mathbf{i},1} n_{\mathbf{i},2} + t \left(\sum_{\mathbf{i},\boldsymbol{\delta_1}} b^{\dagger}_{\mathbf{i}\pm\boldsymbol{\delta}_1,1} b_{\mathbf{i},1} + \sum_{\mathbf{i},\boldsymbol{\delta_2}} b^{\dagger}_{\mathbf{i}\pm\boldsymbol{\delta}_2,2} b_{\mathbf{i},2} \right) \tag{4.2}$$

[1]This feature comes from the model [6] for $LaCoO_3$ and is not important for the method in general.

Further on, all local quantities are diagonal and the elements are equal, which reduces the problem to scalar form 4.1:

$$\mathbf{\Gamma} = \begin{pmatrix} \Gamma & 0 \\ 0 & \Gamma \end{pmatrix} \tag{4.3}$$

$$\mathbf{G} = \begin{pmatrix} G & 0 \\ 0 & G \end{pmatrix} \tag{4.4}$$

...

The totally empty lattice (vacuum state) is represented by the global LS state $|\emptyset\rangle \equiv \prod_{\mathbf{i}} |\mathrm{LS}_{\mathbf{i}}\rangle$. IS excitations are created by bosonic creation operators $b^{\dagger}_{\mathbf{i},\alpha}|\emptyset\rangle \equiv |\mathrm{IS}_{\mathbf{i},\alpha}\rangle$. Nearest neighbor hopping of the bosons is allowed in direction $\boldsymbol{\delta}_1 \in \{(1,0,0),(0,0,1)\}$ for $|\mathrm{IS}_{\mathbf{i},1}\rangle$ and in direction $\boldsymbol{\delta}_2 \in \{(0,1,0),(0,0,1)\}$ for $|\mathrm{IS}_{\mathbf{i},2}\rangle$ with amplitude t. The local energy of the IS state is ε. If a site is doubly occupied, it is called HS excitation $|\mathrm{HS}_{\mathbf{i}}\rangle \equiv b^{\dagger}_{\mathbf{i},2} b^{\dagger}_{\mathbf{i},1}|\emptyset\rangle$. In the definition of the HS state the Pauli principle can already be seen. As discussed in chapter 2 underlying electrons force the bosons to obey hard-core constraints of maximum one boson of a given flavor. Here the focus is on the two possibilities how hard-core constraints can be enforced. Figure 4.2 compares occupation densities of simulations with explicit hard-core constraint with ones obtained with dynamical hard-core constraint. The latter is introduced by an additional on-site interaction term $U/2 \sum_{\mathbf{i}} [\sum_{\alpha} (n_{\mathbf{i}\alpha} - 1) n_{\mathbf{i}\alpha}]$. The important difference between the amplitudes U and V has to be emphasized here. On-site repulsion U is the parameter which ensures dynamical hard-core constraints and can also be found in the Bose-Hubbard Hamiltonian equation 2.7, in contrast to that, parameter V controls the on-site interaction between bosons of different flavors. We use V to simulate on-site attraction between IS states of different flavors which therefore build HS states. The parameters are chosen as: $\varepsilon = 0.34$, $t = 0.058$, $V = 0.62$ [7] found for $LaCoO_3$. Inverse temperature is set to $\beta = 20$.

We show occupation densities of IS states (n) and HS states (n_{HS}) as a function of on-site repulsion U in figure 4.2. It is found, that in the limit $U \to \infty$ occupation densities with dynamical hard-core constraints reach the values for explicit constraints asymptotically. For $U = 5$ the occupation density with dynamical constraint is 6.9 % bigger than in explicit case, while for $U = 20$ it is only 1.7 % bigger. Furthermore we find, that IS states populate some sites alone, but many of them build HS states, as it is energetically favorable. For the moment it shall be pointed out, that the convergence of dynamical HC constraint to explicit one can be studied well in imaginary time Greens function, this will be discussed in more detail below, for example in figures 4.5a and 4.5b.

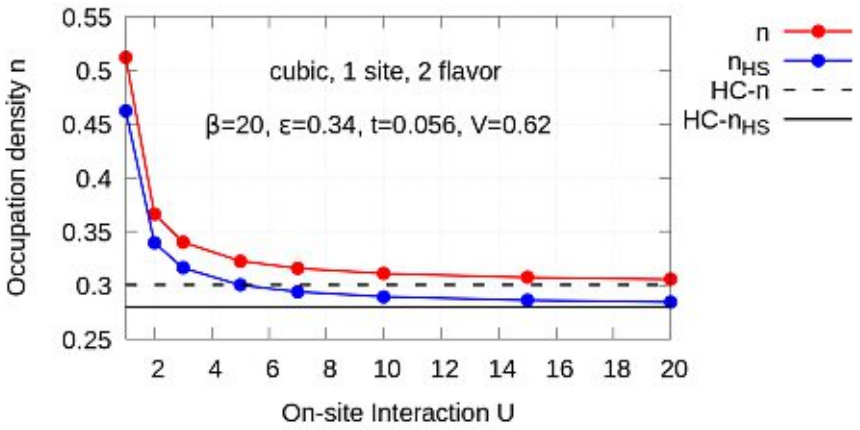

Figure 4.2: Occupation densities n and n_{HS} are calculated within CT-QMC calculation for different on-site interactions U and plotted in comparison with explicit hard-core constraint calculations.

4.2 Non-Degenerate Exciton Energy Levels

After reproducing the data of Ref [6] with scalar rescaling factor we now extend $\mathbf{\Gamma}$ and other local quantities in a first step to diagonal matrices with unequal entries.

$$\mathbf{\Gamma} = \begin{pmatrix} \Gamma_{11} & 0 \\ 0 & \Gamma_{22} \end{pmatrix} \tag{4.5}$$

$$\mathbf{G} = \begin{pmatrix} G_{11} & 0 \\ 0 & G_{22} \end{pmatrix} \tag{4.6}$$

...

This is done via flavor dependent on-site energy ε_α. Studies are done with the simplest model covering the necessary parameters. We use a one dimensional mono atomic chain with two different orbital flavors per site. A sketch is shown in figure 4.3 and the different hopping parameters are directly given in the Hamiltonian:

$$\begin{aligned} H = & \, 0.6 \sum_i n_{i,1} + 0.16 \sum_i n_{i,2} \\ & - 0.5 \sum_i n_{i,1} n_{i,2} \\ & - 0.25 \sum_i b^\dagger_{i\pm1,1} b_{i,1} \pm 0.01 \sum_i b^\dagger_{i\pm1,2} b_{i,1} \\ & + 0.06 \sum_i b^\dagger_{i\pm1,2} b_{i,2} \mp 0.01 \sum_i b^\dagger_{i\pm1,1} b_{i,2} \end{aligned} \tag{4.7}$$

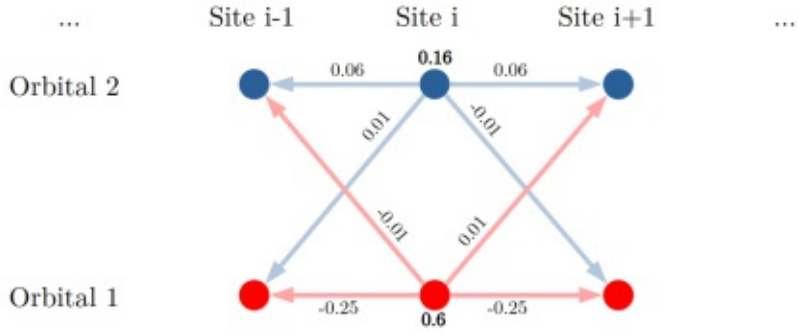

Figure 4.3: Mono atomic chain with two orbital flavors per site. On-site energy and hopping amplitudes are noted in the sketch.

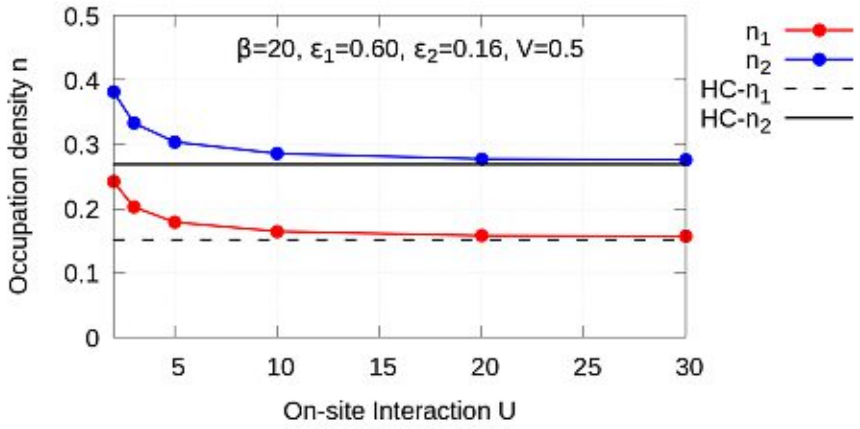

Figure 4.4: Occupation for non-degenerate on-site energies ε_α as a function of U. Convergence to explicit HC constraint is shown.

Convergence of dynamical to explicit hard core constraint is shown for orbital-dependent occupation numbers in figure 4.4. On-site attraction $V = 0.5$ (equal to HS energy $\mathcal{E} = 0.26$) controls the total amount of excitations in the system. Further we study the impact of the different HC constraints on imaginary time Greens function $\mathbf{G}(\tau)$. Equation 2.10 shows that the Greens function is the expectation value of the time ordered combinations of creation and annihilation operators. As the occupations for the orbitals are different we also find different $G_{\alpha\alpha}(\tau)$. In figures 4.5a and 4.5b upper graph labeled with G_{11} corresponds to orbital 1 while lower graph G_{22} corresponds to orbital 2. Note that the local Greens function $G_{12} = 0$ due to the symmetry of the cross-hopping terms. The same is not true for $\mathbf{G}_k$, which is a general 2×2 matrix. Figure 4.5a shows full range of the Greens func-

tion over imaginary time τ from 0 to β, it is periodic with this interval. We find, that dynamical $\mathbf{G}$ and explicit $\bar{\mathbf{G}}$ are matching for almost all times, except $\tau \sim 0^+$. Taking a closer look to $\mathbf{G}(\tau = 0^+)$ shows that functions with dynamical hard-core constraints fulfill $\mathbf{G}(0^+) = -\langle n \rangle_\alpha - 1$. Since the occupancy $\langle n \rangle_\alpha$ depends on U for small values of U two dashed horizontal lines are shown. The value obtained with explicit hard-core constraint $\bar{G}_{\alpha\alpha}(0^+) = -\langle n \rangle_\alpha - (1 - 2\langle n \rangle_\alpha) = -\langle n \rangle_\alpha - \Gamma_{\alpha\alpha}$. In order to calculate rescaling factor one takes this value and $G_{\alpha\alpha}(\beta^-) = -\langle n \rangle_\alpha$ for both dynamical and explicit hard-core constraint, as written in equation 3.11. One can directly read of $\Gamma_{\alpha\alpha}$ in figure 4.5a indicated with arrows. Figure 4.5b enables a more detailed view to low τ and shows the pointwise convergence of $\mathbf{G}(\tau) \to \bar{\mathbf{G}}(\tau)$ on $(0, \beta]$ with increasing U, but $\tau = 0$ is excluded.

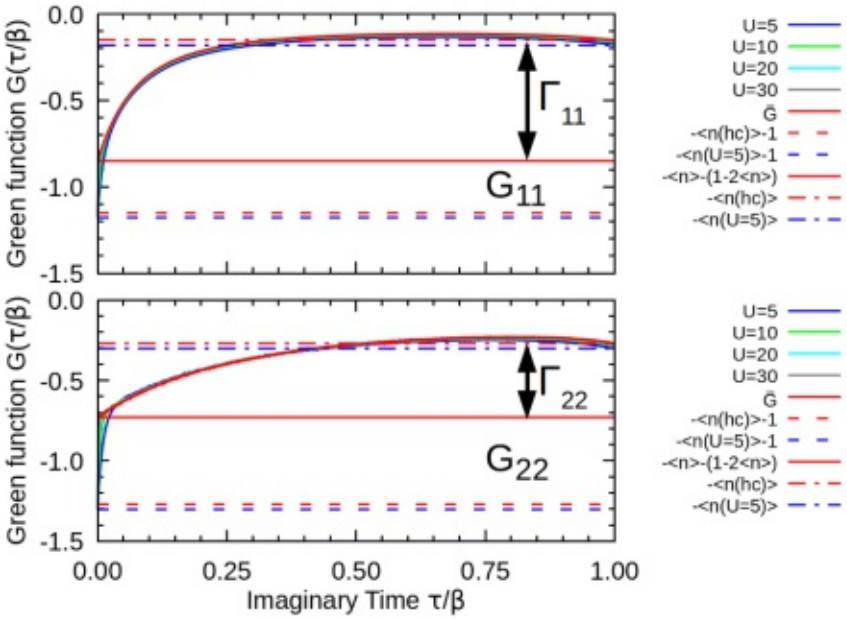

(a) Imaginary time Greens function for one full period 0 to τ. Upper graph corresponds to orbital 1 while lower one corresponds to orbital 2. $\mathbf{G}(\tau)$ is shown for $U = 5, 10, 20$ and 30 and $\bar{\mathbf{G}}(\tau)$ for explicit hard-core constraints. Furthermore left boundary conditions $G_{\alpha\alpha}(0^+) = -\langle n\rangle_\alpha - 1$ and $\bar{G}_{\alpha\alpha}(0^+) = -\langle n\rangle_\alpha - (1 - 2\langle n\rangle_\alpha)$ as well as right one $G_{\alpha\alpha}(\beta^-) = \bar{G}_{\alpha\alpha}(\beta^-) = -\langle n\rangle_\alpha$ are indicated.

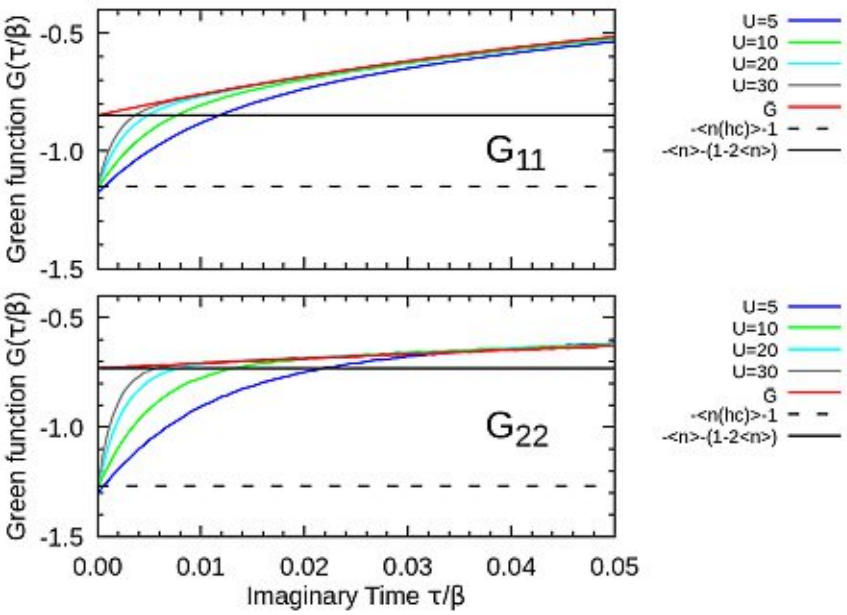

(b) Features for imaginary time close to zero for dynamical hard-core constraint converge pointwise to explicit hard-core results with increasing U.

Figure 4.5: $\mathbf{G}(\tau)$ and $\bar{\mathbf{G}}(\tau)$ in diagonal basis.

4.2.1 Breakdown of Dyson-Mori Form

The model is also used to demonstrate connection between rescaling $\mathbf{\Gamma}$ and k-integrated spectral density $-\frac{1}{\pi}\Im\bar{\mathbf{G}}(\omega)$ discussed in chapter 3. Spectral density shows boson specific behaviour, where it is negative for negative values of ω. This fact makes it possible to get negative values for $\mathbf{\Gamma}$ by equation 3.10. Figure 4.6 gives an insight how $\bar{\mathbf{G}}(\tau)$ changes from $n < 0.5$ to $n > 0.5$. These results come from model discussed in detail in section 4.5.

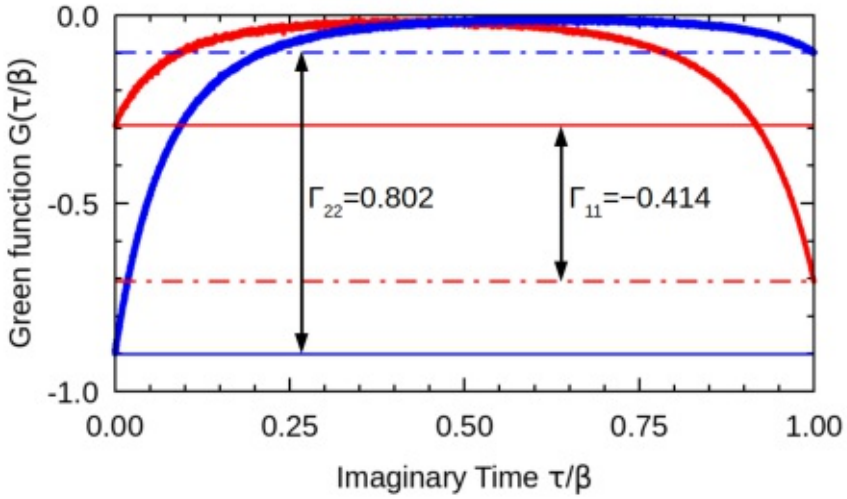

Figure 4.6: Explicit HC Greens function $\bar{\mathbf{G}}(\tau)$ for two different occupation densities. Blue curve shows behavior known from figure 4.5a. Rescaling factor Γ_{22} for occupation $n = 0.09921$ is calculated as value of the dashed blue line minus value of the solid blue line. Also the red case is possible, where Γ_{11} becomes negative (dashed red minus solid red) for $n = 0.70713$. This is visible by the boundary points of $\bar{\mathbf{G}}(\tau)$.

A special case $n = 0.5$ will be discussed, as implementation of HB-DMFT with $\underline{\mathbf{\Gamma}}$ in equation 3.15 comes to its limits in this case. Therefore figure 4.7 acts as example. We use here a single site model, with which it is easier to tune parameters. To see with bare eye that the amount of spectral density is equal for negative and positive energies the curve in figure 4.7 is copied and multiplied by -1. This leads to a vanishing integral of spectral density over ω, so $\mathbf{\Gamma} = 0$ and inverse, which is necessary for equation 3.13, is not defined. To be not affected by this, more general implementation with equation 3.9 is used. Note, that $\mathbf{G}_k$ exhibits $1/\omega^2$ behavior for large U in this case.

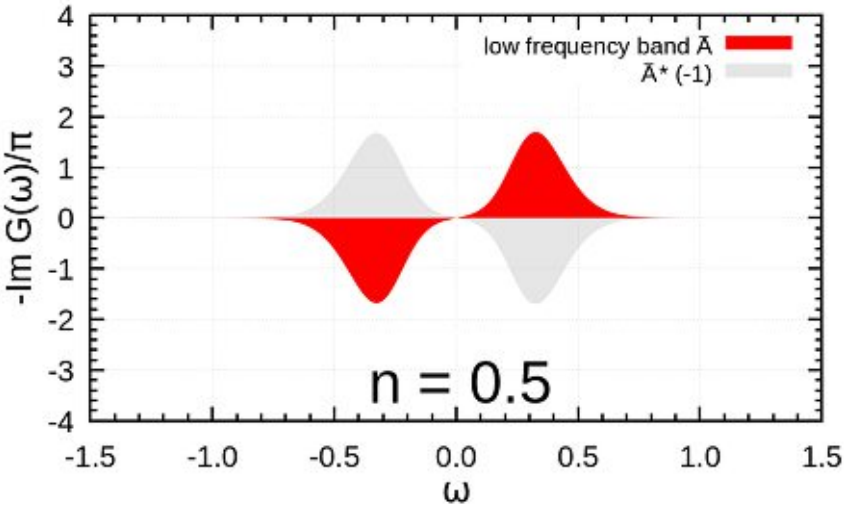

Figure 4.7: Local spectral density for half filled system. Occupation density $n = 0.5$ leads to vanishing rescaling factor.

4.3 General Local Quantities

Until this point all local quantities (Greens function, self energy, hybridization function, rescaling, etc.) have diagonal form. In order to study results also for more general systems and appropriate Hamilton operators, the DMFT simulation program is extended and tested in this section. We stick to one dimensional single atomic chain, where orbitals differ in on-site energies and hopping amplitudes to neighboring sites.

4.3.1 Off-Diagonal by Basis Rotation

Off-diagonal quantities are studied with the known system from previous section. To get off-diagonal Greens functions a unitary basis transform is performed. In the following we indicate to the transformation of annihilation, creation and occupation number operator. Elements of the old basis are denoted with i, j while elements of the new basis are denoted with primed letters i', j'. Here, $\mathbf{U}$ is a unitary matrix $\mathbf{U}\mathbf{U}^\dagger = 1$ with elements $U_{ij'} = \langle i|j'\rangle$. Creation and annihilation operator transform as

$$d^\dagger_{i'} = \sum_i U_{ii'} c^\dagger_i \tag{4.8}$$

$$d_{i'} = \sum_i (\mathbf{U}^\dagger)_{i'i} c_i \tag{4.9}$$

which leads to the transformation of the occupation number operator:

$$d^\dagger_{i'} d_{j'} = \sum_{i,j} U_{ii'} c^\dagger_i c_j (\mathbf{U}^\dagger)_{j'j}$$
$$\mathbf{U}^T c^\dagger_i c_j (\mathbf{U}^\dagger)^T \tag{4.10}$$

Advantage of using a system, which is reducible to diagonal basis is that it can be transformed back at any step of the DMFT cycle and results can be verified. To obtain results in figures 4.8b, 4.9 and 4.10 diagonal system is rotated with real unitary matrix:

$$\mathbf{U} = \begin{pmatrix} \cos(\pi/4) & -\sin(\pi/4) \\ \sin(\pi/4) & \cos(\pi/4) \end{pmatrix} = \begin{pmatrix} 1/\sqrt{2} & -1/\sqrt{2} \\ 1/\sqrt{2} & 1/\sqrt{2} \end{pmatrix} \tag{4.11}$$

Thereby diagonal elements of the Greens function are mixed and off-diagonal elements G_{12} and G_{21} appear. In order to demonstrate the impact of basis rotation, figures 4.8a and 4.8b show occupation density as a function of wave number $\langle n \rangle_{\alpha\beta}(k)$. With the definition of orbital dependent occupation number:

$$\langle n \rangle_{\alpha\beta} = \langle b^\dagger_\beta b_\alpha \rangle \tag{4.12}$$

Left figure shows the diagonal system, where $\langle n \rangle_{12} = \langle n \rangle_{21} = 0$ for all k. On one hand data for right figure are obtained after a DMFT cycle with rotated basis. Parts of the occupation density are moved to off-diagonal elements. On the other hand the same result is achieved by deploying equation 4.10 to diagonal k resolved occupation density. This check clearly confirms the correct implementation of off-diagonal quantities.

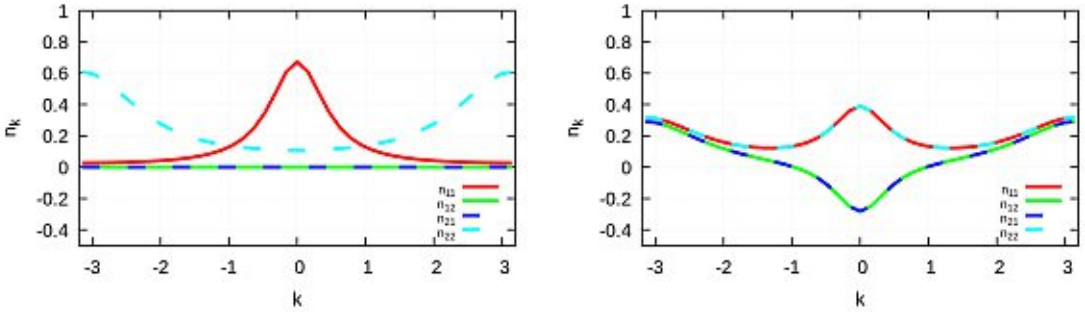

(a) Diagonal occupation density.

(b) Off-diagonal occupation density.

Figure 4.8: Performing an unitary basis transform is demonstrated by k resolved occupation densities $n(k)$. In case (a) off-diagonal elements are equal zero, while case (b) shows mixed orbitals.

Focusing on Greens function 4.9 one can directly read of rescaling matrix $\mathbf{\Gamma}$, also for off-diagonal elements G_{12} and G_{21}. Boundary values for off-diagonal elements can not be identified with occupation number of an orbital but with mixed annihilation and creation operators $\langle b_\alpha^\dagger b_\beta \rangle$ with $\alpha \neq \beta$. Again a more detailed view to low τ in figure 4.10 gives information of the pointwise convergence of dynamical to explicit hard-core constraints. Here $\bar{\mathbf{G}}(\tau = 0^+)$ switches sign compared to $\mathbf{G}(\tau = 0^+)$ so that rescaling can be calculated with equation 3.11.

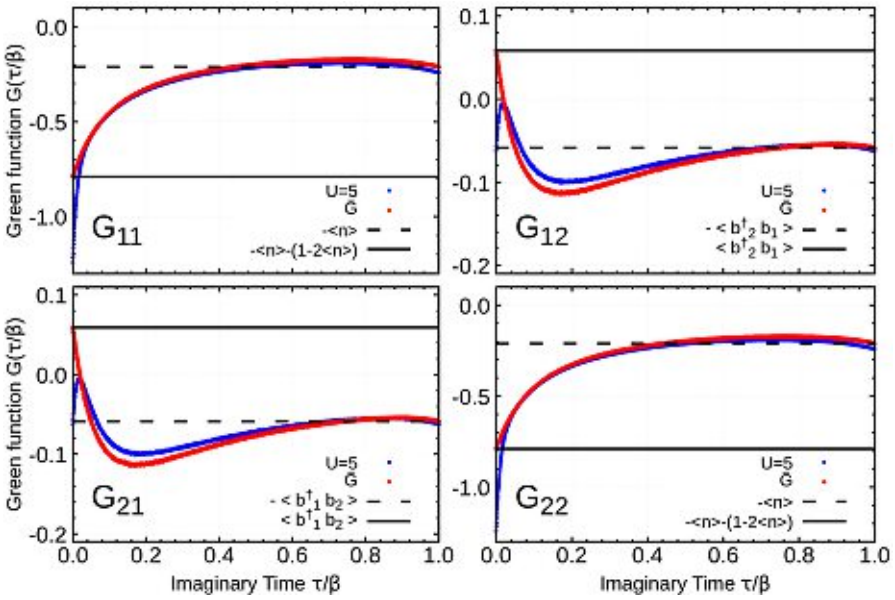

Figure 4.9: Greens functions $\mathbf{G}(\tau)$ and $\bar{\mathbf{G}}(\tau)$ in rotated basis. Figures are arranged in matrix form. Features differ for $\mathbf{G}(\tau = 0^+)$ and $\bar{\mathbf{G}}(\tau = 0^+)$ in diagonal as well as in off-diagonal elements.

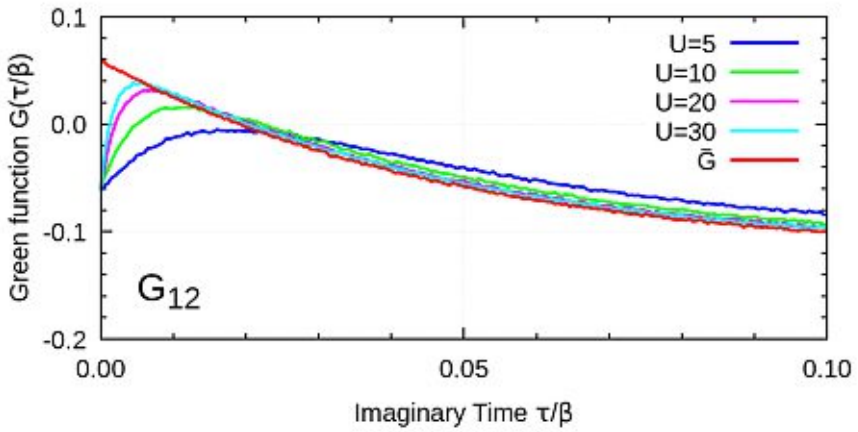

Figure 4.10: Results for dynamical HC constraints $\mathbf{G}(\tau)$ converge pointwise with increasing U to $\bar{\mathbf{G}}(\tau)$.

4.3.2 General Off-Diagonal Hybridization

With the experience of hard-core bosonic DMFT performed with diagonal systems and systems which are reducible to diagonal ones we will show here Greens functions for irreducible off-diagonal systems i.e., a model in which the hybridization function $\mathbf{\Delta}(\omega)$ cannot be made diagonal by an ω-independent unitary transformation. We reach such a system by breaking the symmetry of cross-hopping parameters for left and right neighbors in the mono atomic chain. This leads to the following Hamiltonian:

$$\begin{aligned} H = & \, 0.6 \sum_i n_{i,1} + 0.16 \sum_i n_{i,2} \\ & - 0.5 \sum_i n_{i,1} n_{i,2} \\ & - 0.25 \sum_i b^\dagger_{i\pm1,1} b_{i,1} + 0.01 \sum_i b^\dagger_{i+1,2} b_{i,1} - 0.1 \sum_i b^\dagger_{i-1,2} b_{i,1} \\ & + 0.06 \sum_i b^\dagger_{i\pm1,2} b_{i,2} - 0.1 \sum_i b^\dagger_{i+1,1} b_{i,2} + 0.01 \sum_i b^\dagger_{i-1,1} b_{i,2} \end{aligned} \tag{4.13}$$

Note that the hermeticity is preserved. Even though necessary implementations for a system with these properties for CT-QMC impurity solver are not finished yet for explicit HC constraints we already prepared $\mathbf{G}(\tau)$ in figure 4.11 with finite U. Greens function is shown for different values of on-site repulsion U and we find a trend with increasing U, which has to be confirmed in further simulations.

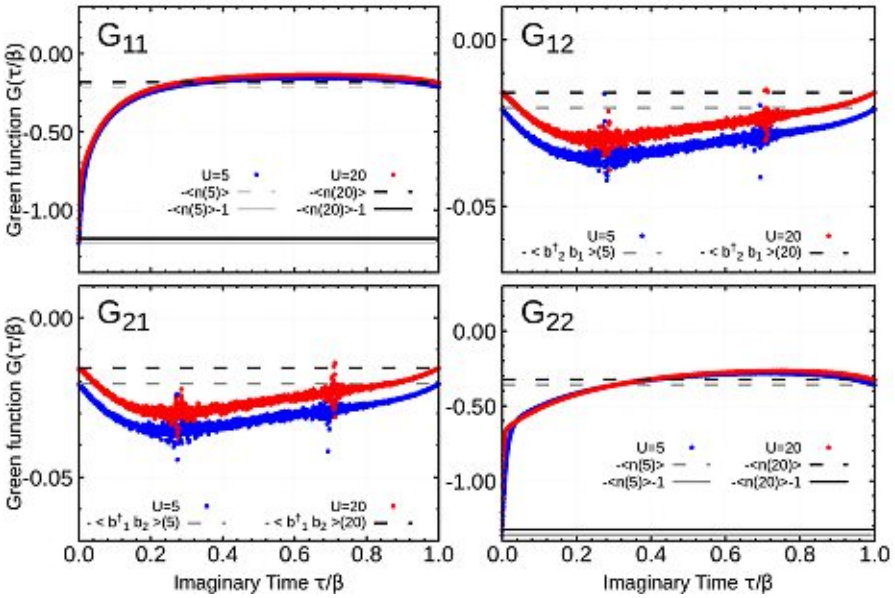

Figure 4.11: Greens function $\mathbf{G}(\tau)$ for a system with off-diagonal hybridization. The trend of the features has to be confirmed by explicit HC calculations.

4.4 Site Dependent Attraction V

In this section we return to the system of section 4.1 but make the attraction V site dependent. This makes it possible to study how site dependent on-site attraction V_s affects IS occupation density n. We find, and this will be extended in the next section, that the occupation is a function of on-site attraction $n(V)$. For the needed adaptions lattice part of DMFT cycle needs to be adjusted as unit vectors and inverse unit vectors change due to new setup of neighboring sites, see figure 4.12 for the changed geometries. In the Hamiltonian (equation 4.14) orbital flavors have to be understood in terms of primed coordinate system $\{x', y'\}$. The two different on-site attractions V_s enter in this two site case via its uniform $\bar{V} = (V_1 + V_2)/2$ and staggered $\Delta = |\bar{V} - V_s|$ parts. Furthermore impurity part has to be solved for each site in the unit cell separately.

$$H = \varepsilon \sum_{\mathbf{i}} \sum_{\alpha} n_{\mathbf{i},\alpha} - \sum_{\mathbf{i}} [\bar{V} + (-1)^{|\mathbf{i}|}\Delta] n_{\mathbf{i},1} n_{\mathbf{i},2}$$
$$+ t \left(\sum_{\mathbf{i},\boldsymbol{\delta_1}} b^{\dagger}_{\mathbf{i}\pm\boldsymbol{\delta}_1,1} b_{\mathbf{i},1} + \sum_{\mathbf{i},\boldsymbol{\delta_2}} b^{\dagger}_{\mathbf{i}\pm\boldsymbol{\delta}_2,2} b_{\mathbf{i},2} \right); \quad |\mathbf{i}| = i + j + l \tag{4.14}$$

The data for figure 4.13 is gathered with $V_1 = 0.61$, therefore HS energy $\mathcal{E}_1 =$

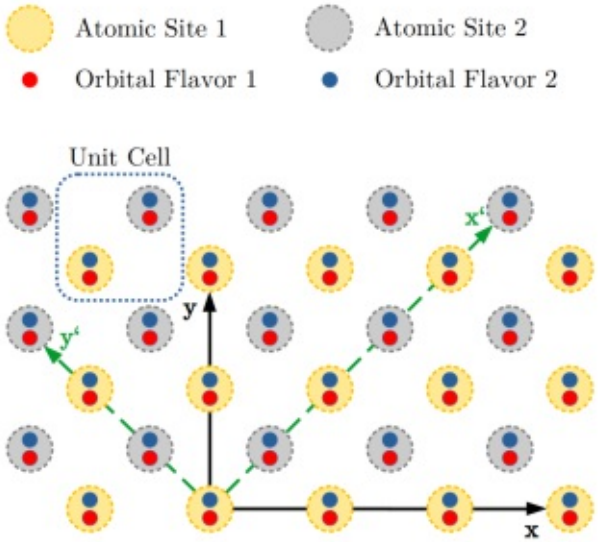

Figure 4.12: An extension to figure 4.1 with two atomic sites per unit cell is shown here. Parameters for different sites can be tuned independently. As a direct consequence bosons have different nearest neighbors and hopping directions are rotated from x and y to x' and y'. For the three dimensional case the same rotation is done in z-direction

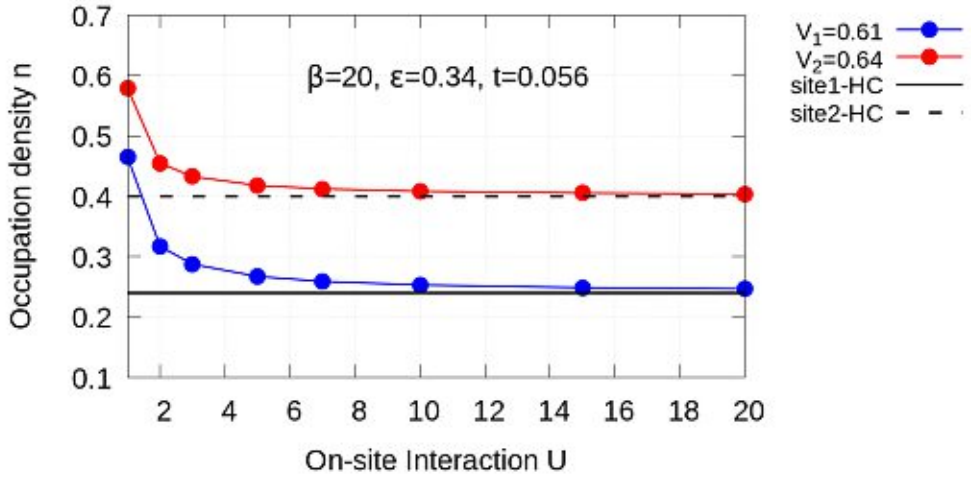

Figure 4.13: IS occupation for model with site dependent attraction V

0.07 and $V_2 = 0.64 \rightarrow \mathcal{E}_2 = 0.04$. For constant temperature, noted as inverse temperature $\beta = 20$, one clearly finds, that lower HS energy leads to more occupied sites. Also for this more complex setting we find very good consensus between dynamical and explicit HC constraints for the limit $U \rightarrow \infty$.

4.5 Spontaneous Spin-State Order

In the previous section we have introduced the two-sublattice order by mean of staggered interaction. Similar arrangement can take place also in a model with uniform interaction due to spontaneous symmetry breaking. This situation, which is physically relevant for $LaCoO_3$, is studied in this section. We will refer to the state with unequally occupied sublattices as spin-state order (SSO) and the uniform occupation as normal state. The transition between the two is a phase transition which can be driven by a change of coupling constants or temperature. We use 4.14 on a square lattice, i.e., $\mathbf{i} = i(1,0) + j(0,1)$ and $\boldsymbol{\delta}_1 = (1,0), \boldsymbol{\delta}_2 = (0,1)$ in this study. Our aim of investigations is spontaneous appearance of the arrangement of LS and HS states on the lattice driven by the choice of V with condition $V_1 = V_2$.
We choose low temperature $\beta = 40$ and hopping amplitude $t = 0.116$. IS energy $\varepsilon = 0.34$ is kept fixed. Varying the on-site attraction V to higher values clearly leads to different occupation of sites, SSO appears, as site 1 is occupied with IS states and site 2 is empty with IS state, therefore occupied with LS states mainly, see figure 4.14. A checkerboard pattern appears.

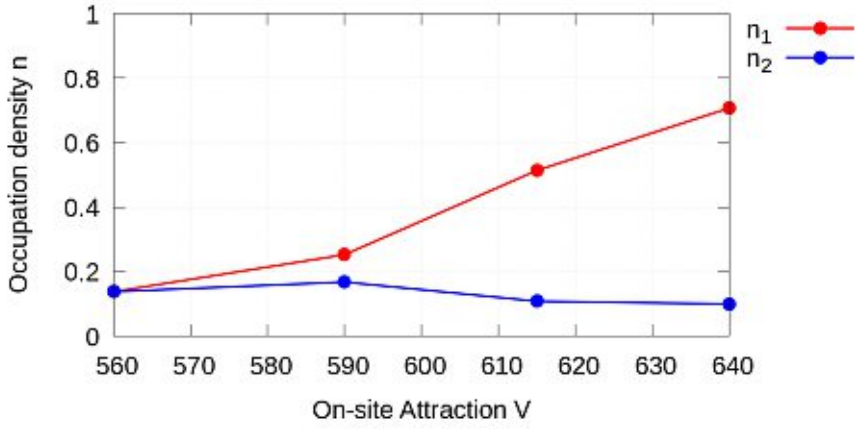

Figure 4.14: With increasing on-site attraction SSO phase appears spontaneously.

I will show spectral densities for different occupation densities ($n < 0.5$ and $n > 0.5$) and demonstrate how explicit HC constraint affects them.
Local spectral densities as in figure 3.1 are shown for real calculations with dynamical HC constraints in figure 4.15. There can clearly be distinguished between lower frequency band $\bar{\mathbf{A}}(\omega)$ and upper Hubbard band $\mathbf{a}(\omega)$. As on-site repulsion controls the position of $\mathbf{a}(\omega)$ it is settled around $U = 5$ here. Furthermore occupation density gives information about positive and negative amount of spectral density in $\bar{\mathbf{A}}$. More precisely $n < 0.5$ implies more amount of positive and $n > 0.5$ more amount of negative $\bar{\mathbf{A}}$. Upper Hubbard band is always positive so that equation 4.15 is fulfilled.

$$-\frac{1}{\pi}\int_{-\infty}^{\infty} d\omega \Im \mathbf{G}(\omega) \equiv 1 \tag{4.15}$$

For results in figure 4.14 we perform simulations with explicit HC constraint so upper Hubbard band gets cut off. This cut-off violates equation 4.15 and one finds $\mathbf{\Gamma}$ with equation 3.10. For the data points in figure 4.14 the corresponding local spectral densities are shown in figure 4.16. The two different sites are shown in each sub-figure and normal or SSO phase can be read off directly from the spectral density. We have checked the convergence of occupation numbers obtained with dynamical constraint to their HC counterparts.
Another way to visualize the convergence of dynamical to explicit HC constraint is the k-resolved spectral function. Plots in figure 4.17 show spectral densities for $V = 640$, which correspond to the k-integrated data in figure 4.16d. The exact same system is shown in figures 4.16d and 4.17d in different representations. The latter one shows data for different k-points along high symmetry lines of the lattice. The color scheme represents amplitudes and y-axes indicates frequency ω. With

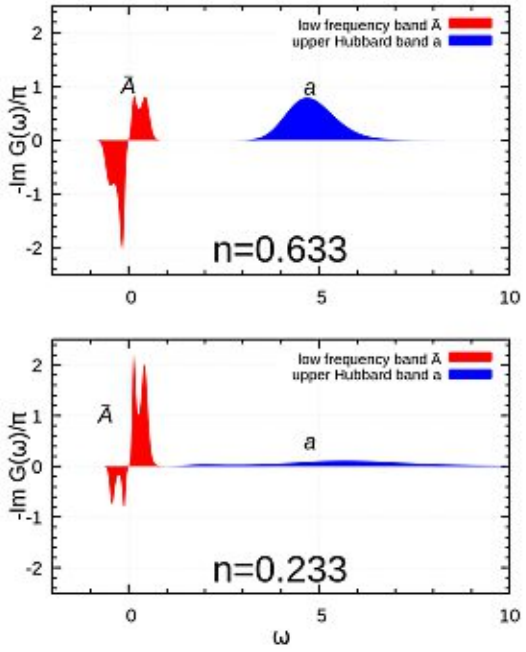

Figure 4.15: Local spectral densities for two dimensional model with two sites in unit cell for on-site repulsion U=5, V=640

increasing U site 1 gets more negative amount of spectral density and site 2 gets more amount of positive spectral density.

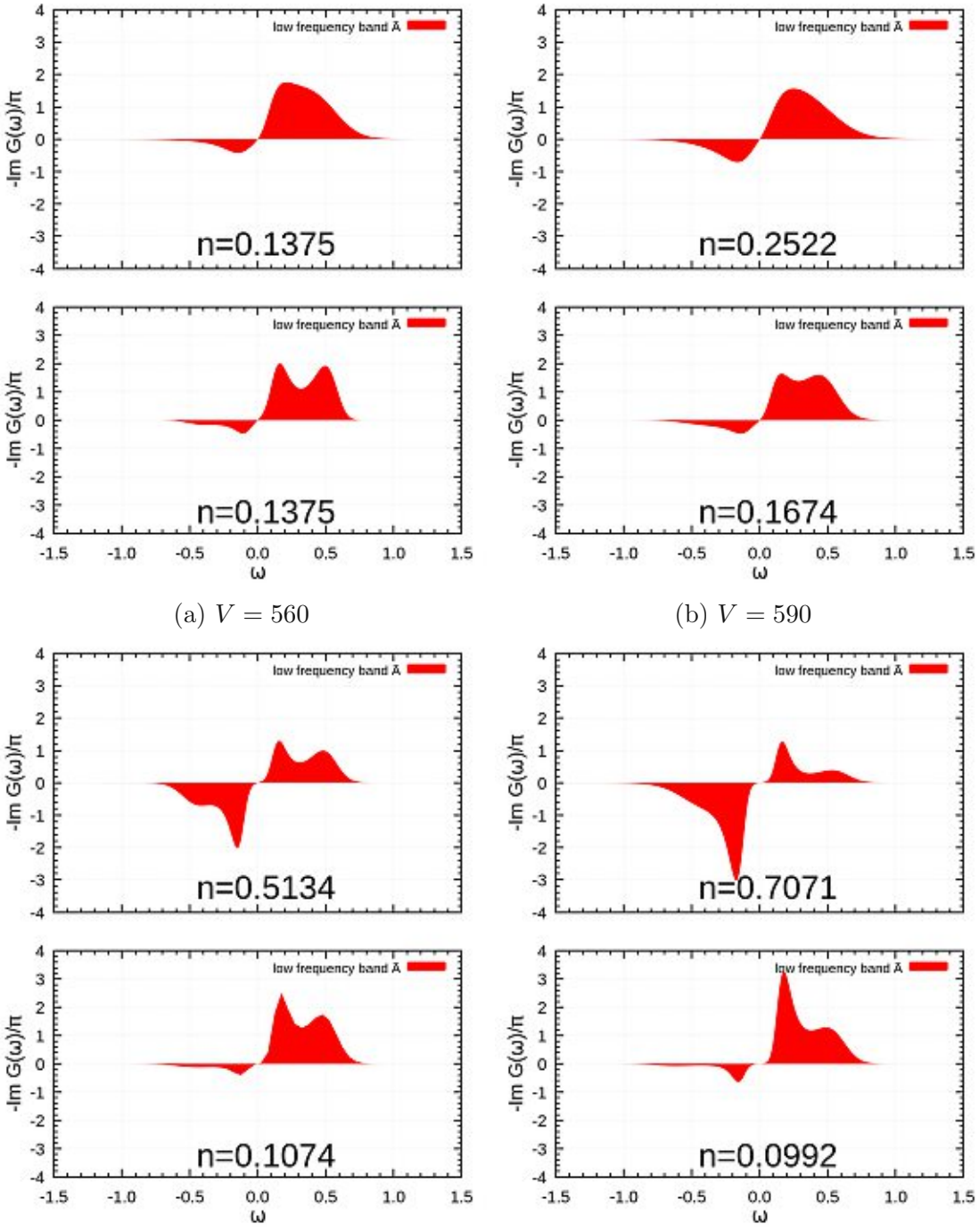

(a) $V = 560$ (b) $V = 590$

(c) $V = 615$ (d) $V = 640$

Figure 4.16: Local spectral densities on the two sublattices corresponding to on-site attraction in figure 4.14.

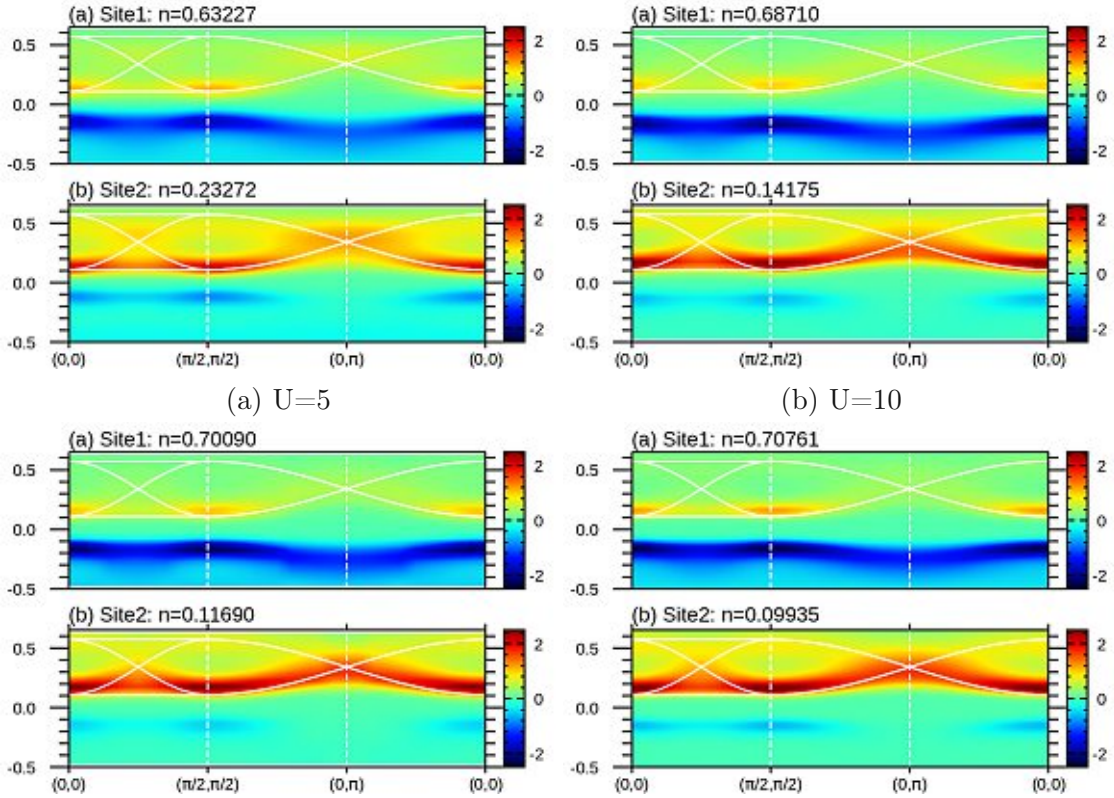

(a) U=5 (b) U=10

(c) U=20 (d) HC

Figure 4.17: Local k-resolved spectral functions for different finite U values and explicit HC constraint. Data in (d) corresponds to k-integrated spectral density in figure 4.16d.

5 Conclusions

In summary, we presented a dynamical mean-field theory for hard-core bosons (HB-DMFT). Therefore broken canonical commutation relations are implemented to the B-DMFT cycle following Anders und Gull [22] and tested in several lattice models. We raised complexity of local quantities from scalar (state of the art results in [6]) to diagonal matrix form $\mathbf{M} = \mathrm{diag}[M_{11}, M_{22}]$ in the first step and further on to full matrix form. Thus it is possible to formulate the theory analogous to Dyson-Mori form developed by Shastry [20, 21] for t-J model.
The HC bosonic formulation has numerical advantages over the dynamical implementation of the constraint. First, the steep feature in $\mathbf{G}(\tau)$ at $\tau = 0^+$ or $\tau = \beta^-$ vanishes in the HC formulation, accuracy in τ-mesh can be reduced. Second, in Fourier transformed quantities one can perform a cut-off for high frequencies as auxiliary self energy reaches its asymptotic behavior outside the support of low frequency band $\bar{\mathbf{A}}$. This leads to a reduction of numerical effort.
Even though implementation in Dyson-Mori form is possible, we showed, that it is not generally applicable for bosonic DMFT as the rescaling fails for half filled lattices. Therefore implementation with universal formulation of k-summed Greens function, as discussed in chapter 3 is necessary.
In the last section we have investigated and described a phase transition from normal (uniform occupied sublattices) to SSO (unequal occupation) state, driven by a change of coupling constants.
For future work one can also monitor the phase transition for different temperatures and in three dimensional case, as well as condensate can be included.

List of Figures

Bibliography

[1] R. R. Heikes, R. C. Miller, and R. Mazelsky. "Magnetic and electrical anomalies in $LaCoO_3$". In: *Physica* 30 (1964), p. 1600. DOI: 10.1016/0031-8914(64)90182.

[2] A. Sotnikov, K. Ahn, and J. Kuneš. "Ferromagnetism of $LaCoO_3$ films". In: *SciPost Phys.* 8 (6 2020), p. 82. DOI: 10.21468/SciPostPhys.8.6.082.

[3] S. Bühler-Paschen and P. Mohn. *Festkörperphysik 2*. lecture notes. Vienna University of Technology, 2016.

[4] Y. Tanabe and S. Sugano. "On the Absorption Spectra of Complex Ions II". In: *Journal of the Physical Society of Japan* 9.5 (1954), p. 766. DOI: 10.1143/JPSJ.9.766.

[5] G. Racah. "Theory of Complex Spectra. II". In: *Phys. Rev.* 62 (9-10 Nov. 1942), pp. 438–462. DOI: 10.1103/PhysRev.62.438.

[6] A. Hariki, R. Wang, A. Sotnikov, K. Tomiyasu, D. Betto, N. B. Brookes, Y. Uemura, M. Ghiasi, F. M. F. de Groot, and J. Kuneš. "Damping of spinful excitons in $LaCoO_3$ by thermal fluctuations: Theory and experiment". In: *Phys. Rev. B* 101 (24 June 2020), p. 245162. DOI: 10.1103/PhysRevB.101.245162.

[7] R. Wang, A. Hariki, A. Sotnikov, F. Frati, J. Okamoto, H. Huang, A. Singh, D. Huang, K. Tomiyasu, C. Du, J. Kuneš, and F. de Groot. "Excitonic dispersion of the intermediate spin state in $LaCoO_3$ revealed by resonant inelastic x-ray scattering". In: *Phys. Rev. B* 98 (3 July 2018), p. 035149. DOI: 10.1103/PhysRevB.98.035149.

[8] S. Bose. "Plancks Gesetz und Lichtquantenhypothese". In: *Zeitschrift für Physik* 26 (Dec. 1924), pp. 178–181. DOI: 10.1007/BF01327326.

[9] A. Einstein. "Quantentheorie des einatomigen idealen Gases". In: *Sitzungsberichte der Preußischen Akademie der Wissenschaften* (1924/25).

[10] E. Pavarini, E. Koch, and S. Zhang, eds. *Many-Body Methods for Real Materials*. Vol. 9. Schriften des Forschungszentrums Jülich. Modeling and Simulation. Jülich: Forschungszentrum Jülich GmbH Zentralbibliothek, Verlag, Sept. 2019, getr. Zählung. ISBN: 978-3-95806-400-3.

[11] J. Hubbard. "Electron Correlations in Narrow Energy Bands". In: *Proceedings of the Royal Society of London. Series A, Mathematical and Physical Sciences* 276.1365 (1963), pp. 238–257. ISSN: 00804630.

[12] A. Georges, G. Kotliar, W. Krauth, and M. J. Rozenberg. "Dynamical mean-field theory of strongly correlated fermion systems and the limit of infinite dimensions". In: *Rev. Mod. Phys.* 68 (1 Jan. 1996), pp. 13–125. DOI: 10.1103/RevModPhys.68.13.

[13] A. Georges and G. Kotliar. "Hubbard model in infinite dimensions". In: *Phys. Rev. B* 45 (12 Mar. 1992), pp. 6479–6483. DOI: 10.1103/PhysRevB.45.6479.

[14] W. Metzner and D. Vollhardt. "Correlated Lattice Fermions in $d = \infty$ Dimensions". In: *Phys. Rev. Lett.* 62 (3 Jan. 1989), pp. 324–327. DOI: 10.1103/PhysRevLett.62.324.

[15] G. Kotliar and D. Vollhardt. "Strongly Correlated Materials: Insights From Dynamical Mean-Field Theory". In: *Physics Today - PHYS TODAY* 57 (Mar. 2004), pp. 53–59. DOI: 10.1063/1.1712502.

[16] P.C. Anders. "Dynamical Mean-Field Theory for Bosons and Bose-Fermi Mixtures". PhD thesis. 2011. DOI: 10.3929/ETHZ-A-007146448.

[17] E. Gull. "Continuous-Time Quantum Monte Carlo Algorithms for Fermions". PhD thesis. 2008. DOI: 10.3929/ETHZ-A-005722583.

[18] L. Boehnke, H. Hafermann, M. Ferrero, F. Lechermann, and O. Parcollet. "Orthogonal polynomial representation of imaginary-time Green's functions". In: *Physical Review B* 84.7 (Aug. 2011). ISSN: 1550-235X. DOI: 10.1103/physrevb.84.075145.

[19] H. Hafermann, K. R. Patton, and P. Werner. "Improved estimators for the self-energy and vertex function in hybridization-expansion continuous-time quantum Monte Carlo simulations". In: *Physical Review B* 85.20 (May 2012). ISSN: 1550-235X. DOI: 10.1103/physrevb.85.205106.

[20] B. S. Shastry. "Extremely correlated quantum liquids". In: *Phys. Rev. B* 81 (4 Jan. 2010), p. 045121. DOI: 10.1103/PhysRevB.81.045121.

[21] B. S. Shastry. "Erratum: Anatomy of the self-energy [Phys. Rev. B 84, 165112 (2011)]". In: *Phys. Rev. B* 86 (7 Aug. 2012), p. 079911. DOI: 10.1103/PhysRevB.86.079911.

[22] P. Anders, E. Gull, L. Pollet, M. Troyer, and P. Werner. "Dynamical mean field solution of the Bose-Hubbard model". In: *Phys. Rev. Lett.* 105 (Sept. 2010). DOI: 10.1103/PhysRevLett.105.096402.

Acknowledgments

Working with this project has been an interesting and pleasant experience, as well as it has been challenging.
First of all I would like to thank my supervisor Jan Kuneš who gave me the possibility to work in his group and under great guidance.
Next I am thankful to Atsushi Hariki for providing the necessary software and supporting this project with all his effort. Here, I also would like to thank Andrii Sotnikov for sharing his data to clarify our point of view about HB-DMFT.
I am grateful to all group members for the help and hints to improve my scientific work.
The computational results presented have been obtained using the Vienna Scientific Cluster (VSC).
On the more personal side, I would like to thank my classmates at university Nicole Jurjew, Daniel Marik, Veronika Pfannenstill, Magdalena Pieler and Rainer Rockenbauer for all the helpful discussions and of course for all the fun we had together. Special thanks go to my parents Erich and Ingrid and my brother Pascal for their constant support in all the years. Finally, I want to thank Maxi for the support and motivation during this work.